Nano Energy (2016) **22**, 48-58

Available online at www.sciencedirect.com

ScienceDirect

journal homepage: www.elsevier.com/locate/nanoenergy

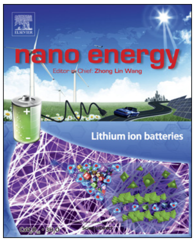

COMMUNICATION

Uniform $8LiFePO_4 \cdot Li_3V_2(PO_4)_3/C$ nanoflakes for high-performance Li-ion batteries

Shuquan Liang[a], Xinxin Cao[a], Yaping Wang[a], Yang Hu[a], Anqiang Pan[a,*], Guozhong Cao[b]

[a]*School of Material Science and Engineering, Central South University, Changsha 410083, Hunan, PR China*
[b]*Department of Materials Science & Engineering, University of Washington, Seattle, WA 98195, USA*

Received 1 October 2015; received in revised form 26 January 2016; accepted 1 February 2016
Available online 8 February 2016

KEYWORDS
Li-ion battery;
Cathode;
$LiFePO_4 \cdot Li_3V_2(PO_4)_3/C$;
Nanoflake;
Surfactant

Abstract

The synthesis of novel nanostructures at high temperatures is a big challenge because of the particle growth and aggregations. In particular, the fabrication of two active components with uniform structures is rarely reported. Herein, uniform $8LiFePO_4 \cdot Li_3V_2(PO_4)_3/C$ nanoflakes have been synthesized by a one-pot, solid-state reaction in molten hydrocarbon, where the oleic acid functions as a surfactant. The composite components of $LiFePO_4$ and $Li_3V_2(PO_4)_3$ are distributed homogenously within the nanoflakes. Moreover, the nanoflakes are coated by *in-situ* generated carbon from oleic acid during the sintering process in H_2/Ar. The as-prepared $8LiFePO_4 \cdot Li_3V_2(PO_4)_3/C$ nanoflakes are approximately 20-50 nm in thickness and are stacked together to construct a porous structure, which have a surface area of 30.21 $m^2\,g^{-1}$. The lithium ion diffusion coefficient can be greatly improved by making $8LiFePO_4 \cdot Li_3V_2(PO_4)_3/C$ composite. As cathode material for lithium ion batteries, the as-prepared material exhibits excellent electrochemical performances, including high reversible capacity, good cyclic stability and rate capability. The composite electrode delivers a high capacity of 161.5 mAh g^{-1} at 0.1C, which is very close to the theoretical capacity. Even at 10C, the electrode can deliver a specific discharge capacity of 118.6 mA h g^{-1}. After the long-term 1000 cycles, the electrodes can still retain 93.21% and 88.7% of its maximum specific discharge capacities at the rates of 2C and 5C, respectively. The results demonstrate the $8LiFePO_4 \cdot Li_3V_2(PO_4)_3/C$ nanoflakes are promising cathode materials for high-performance lithium ion batteries.

© 2016 Elsevier Ltd. All rights reserved.

---

[*] Corresponding author at: School of Materials Science and Engineering, Central South University, Changsha, 410083, Hunan, PR China. Tel.: 86 0731 88836069; fax: 86 0731 88876692.

E-mail addresses: pananqiang@csu.edu.cn (A. Pan), gzcao@u.washington.edu (G. Cao).

http://dx.doi.org/10.1016/j.nanoen.2016.02.002
2211-2855/© 2016 Elsevier Ltd. All rights reserved.

Introduction

Lithium-ion batteries have been the dominant power supplier for high-tech portable electronic devices for decades. However, other future broad applications, such as plug-in hybrid electric vehicles (PHEV) and plug-in electric vehicle (PEV), require further improvements in many perspectives, such as energy density, safety, durability and cost [1-4]. Recently, lithium transition metal phosphates (such as $LiFePO_4$, $LiMnPO_4$, and $Li_3V_2(PO_4)_3$) have been extensively studied for lithium-ion batteries due to their high energy density, long lifespan, and good safety [5-11]. Among these phosphates, olivine structured $LiFePO_4$, firstly proposed as a cathode material for lithium ion battery by Goodenough et al. in 1997 [12], has been commercialized successfully due to its relatively high capacity, thermal stability, environmental benignity and low cost. Nevertheless, some intrinsic drawbacks should be addressed before its applications in transportation and grid energy storage, such as poor electronic conductivity, and low Li-ion diffusion coefficient [13-20]. To date, great efforts have been devoted to improve its electrochemical performance, such as making nanostructured materials [6,7,15,17], carbon coating [15-17,20], and supervalent cation doping [13,14,18].

More recently, making the composites from both active components has attracted much attention. It is reported that the electrochemical properties of $LiFePO_4$ and $LiMnPO_4$ can be remarkably improved by making composites with $Li_3V_2(PO_4)_3$, a fast ion conductor [13,21-23]. The one-dimensional lithium ion diffusion channel for olivine-type structured $LiMPO_4$ (M=Fe, Mn) limits their high rate performance. Monoclinic $Li_3V_2(PO_4)_3$ with an open three-dimensional framework has much higher Li-ion diffusion efficiency and working potentials [17,24,25]. Moreover, the mutual doping of V^{3+} and Fe^{2+} cations in the phosphates occurs in the fabrication process, resulting enhanced electrochemical properties. For examples, V doping in $LiFePO_4$ [13,26] or $LiMnPO_4$ [23], and Mn, Fe doping in $Li_3V_2(PO_4)_3$ [21,23,27] could improve the electrochemical properties of the bulk materials. Although $xLiFePO_4 \cdot yLi_3V_2(PO_4)_3$ composites have been prepared by various approaches including chemical reduction and lithiation method [28], solid-state reaction [21], spray drying method [27], sol-gel method [29], and rheological phase reaction [22], the controllable synthesis of $xLiFePO_4 \cdot yLi_3V_2(PO_4)_3$ with novel nanostructures is rarely reported. The difficult may be raised from the tendency of forming large particles at high temperatures in order to reach a thermodynamical more stable state.

In order to solve this problem, the surrounding condition for the particle growth should be modified [30-32]. Surfactants have been successfully employed to fabricate various nanostructures in the liquid solvent, which can control the growth of the nanostructures [33,34]. However, they are not suitable for high temperature (>500 °C) operation. Recently, a molten hydrocarbon media has been developed to replace the liquid solvent and the surfactant can function as the structural director in the molten media [35,36]. Choi et al. reported the one-step synthesis of $LiMnPO_4$ nanoflakes and Pan et al. reported the fabrication of $Li_3V_2(PO_4)_3$ nanobelts [8,10]. The obtaining of different morphologies was not only determined by the surfactant, but also the target materials themselves. Although nanostructured phosphates have been prepared for sole $LiMnPO_4$ or $Li_3V_2(PO_4)_3$, no work is reported on the preparation of the uniform nanocomposites of two active components, such as $LiFePO_4$ and $Li_3V_2(PO_4)_3$. The difficulty may be attributed to their structural growth priority for different materials.

Herein, uniform $8LiFePO_4 \cdot Li_3V_2(PO_4)_3/C$ nanoflakes have been successfully prepared in a molten media using oleic acid as a surfactant. The $LiFePO_4$ and $Li_3V_2(PO_4)_3$ are homogeneously distributed through the nanoflakes. Moreover, the composite nanoflakes are coated by a carbon layer, which is *in situ* generated in the calcination process at high temperatures. As a cathode material for lithium-ion batteries, the $8LiFePO_4 \cdot Li_3V_2(PO_4)_3/C$ nanoflakes exhibit superior electrochemical performance.

Experimental section

Preparation of $FeC_2O_4 \cdot 2H_2O$ and $VOC_2O_4 \cdot nH_2O$

The ferrous oxalate dihydrate ($FeC_2O_4 \cdot 2H_2O$) was prepared by precipitation reactions according to a previous report [37]. Briefly, $FeSO_4 \cdot 7H_2O$ and $H_2C_2O_4 \cdot 2H_2O$ in a stoichiometric ratio of 1:1 were added into a beaker with 200 ml deionized water under vigorous magnetic stirring at room temperature. Then 5 ml 10% Sulfuric acid was added to the beaker, followed by continuously stirring for another 4 h to form a bright yellow solution. The mixed solution was kept at 40 °C for 2 days before collecting the yellow precipitate by filtering and washed with distilled water for three times. The yellow precipitate was dried in an oven at 80 °C overnight to obtain the bright yellow microcrystalline powder.

Vanadyl oxalate hydrate ($VOC_2O_4 \cdot nH_2O$) as vanadium sources was prepared through a soft chemical route, which was similar to our previous reports [38-40]. In a typical procedure, V_2O_5 and $H_2C_2O_4 \cdot 2H_2O$ were completely dissolved in deionized water at a stoichiometric ratio of 1:3 and continuously stirred at room temperature until the color of the solution changed from yellow to dark-blue, which indicated the change of the valence of vanadium ions in the solution from +5 to +4. Oxalic acid here was used as both a chelating reagent and as a reducing agent. After the solution was dried in an oven at 80 °C for 12 h, $VOC_2O_4 \cdot nH_2O$ was obtained. The reaction may occur as follows:

$$V_2O_5 + 3H_2C_2O_4 \rightarrow 2VOC_2O_4 \rightarrow 2CO_2 + 3H_2O \quad (1)$$

Preparation of $8LiFePO_4 \cdot Li_3V_2(PO_4)_3/C$ Nanoflake Composite, pristine $LiFePO_4/C$ and $Li_3V_2(PO_4)_3/C$

The nanoflake-stacked $8LiFePO_4 \cdot Li_3V_2(PO_4)_3/C$ was synthesized via a one-step, solid-state reaction in molten surfactant-paraffin media. Specifically, $NH_4H_2PO_4$ was milled initially with oleic acid for 1 h using a QM−3B high-energy milling machine, followed by adding paraffin wax under milling for 30 min. Then, $FeC_2O_4 \cdot 2H_2O$ and $VOC_2O_4 \cdot nH_2O$ were added, and milled for 10 min. Finally, $CH_3COOLi \cdot 2H_2O$ was added and milled for another 10 min. The overall molar ratio of Li: Fe: V: P: oleic acid in the milling mixture is 11: 8: 2: 11: 11. The paraffin wax is twice weight of oleic acid. The viscous precursor slurry was dried in oven at 105 °C for 30 min. The obtained mixture was heated in a tube furnace at 750 °C for 8 h under the flowing of the mixture atmosphere of 5%H_2/95%Ar to yield 8$LiFePO_4\cdot Li_3V_2(PO_4)_3$/C nanoflakes. The heating rate was set of 5 °C/min. The evaporated paraffin was collected at the cooler part of the tube furnace during the heat treatment process. For comparison, the pristine $LiFePO_4$/C and $Li_3V_2(PO_4)_3$/C were synthesized using the molar ratios of Li: Fe: P: oleic acid = 1: 1: 1: 1 and Li: V: P: oleic acid = 3: 2: 3: 3 in the milling mixture, respectively, while the other synthesis conditions were kept unchanged.

Material characterization

The crystallographic information was recorded by X-ray diffraction (XRD) measurements using a Rigaku D/max2500 X-ray diffractometer with non-monochromated Cu-Kα (λ = 1.54178 Å) X-ray source. The samples were scanned in the range between 10° and 80° (2θ) with a step size of 0.02°. The morphology of the composites were characterized by a field-emission scanning electron microscope (FESEM, FEI Nova NanoSEM 230) with an accelerating voltage of 20 kV. The transmission electron microscopy (TEM) images and high-resolution transmission electron microscope (HRTEM) images were gathered on transmission electron microscopy (TEM, JEOL JEM − 2100 F) operating at a 200 kV accelerating voltage. Elemental carbon content in the samples were determined by C-S analysis equipment (CS − 2000, Eltar, Germany). The property of carbon layer was analyzed by Raman spectrometer (LabRAM HR800). Specific surface areas were estimated by Brunauer-Emmet-Teller (BET) method using Nitrogen adsorption-desorption (NOVA 4200e, Quantachrome Instruments).

Electrode fabrication and electrochemical measurements

The electrochemical measurements were carried out by assembly of CR2032 coin cells in a glove box (Mbraun, Germany) filled with ultra-high pure argon gas, which use lithium foil as the anode, polypropylene membrane as the separator, and 1.0 M solution of $LiPF_6$ in ethylene carbon (EC)/diethyl carbonate (DEC)/dimethyl carbonate (DMC) (1:1:1, by volume) as electrolyte. The cathode slurry was prepared by dispersing active materials, acetylene black, and polyvinylidene fluoride (PVDF) binder in N-methyl − 2-pyrrolidone (NMP) solution with a weight ratio of 75: 15: 10. The mixed slurry was spread on aluminum foil, and was dried in a vacuum oven at 100 °C overnight prior cells assembly. The cells were first aged for 12 h before charge/discharge to ensure full absorption of the electrolyte into the electrodes. The electrode area was 1.131 cm^2 and the mass loading of the active material was 1- − 1.5 mg cm^{-2}. Cyclic voltammetry (CV) was tested on an electrochemical workstation (CHI604E, China) in the voltage range of 2.5- − 4.5 V (vs. Li/Li^+) and electrochemical impedance spectroscopy (EIS) measurements were performed on a ZAHNER-IM6ex electrochemical workstation (ZAHNER Co., Germany) in the frequency range of 100 kHz to 10mHz on a cell in as-assembled condition. The galvanostatic charge/discharge performances of the electrodes were studied at ambient temperature in a potential range of 2.5- − 4.3 V vs Li/Li^+ with a multichannel battery testing system (LAND CT2001A, China). The cells were charged under constant current and constant voltage (CCCV) mode, which was then discharged under constant current (CC) mode. The constant current charging is followed by a potentiostatic hold at 4.3 V until the current drops to one tenth of charge current. The cells were then discharge to 2.5 V. Here, 1 C refers to 170 mA g^{-1} for the 8$LiFePO_4\cdot Li_3V_2(PO_4)_3$/C composite and pristine $LiFePO_4$/C electrodes, but for pristine $Li_3V_2(PO_4)_3$/C electrodes, 1 C refers to 133 mA g^{-1}. The capacities were calculated based on the weight of active materials only.

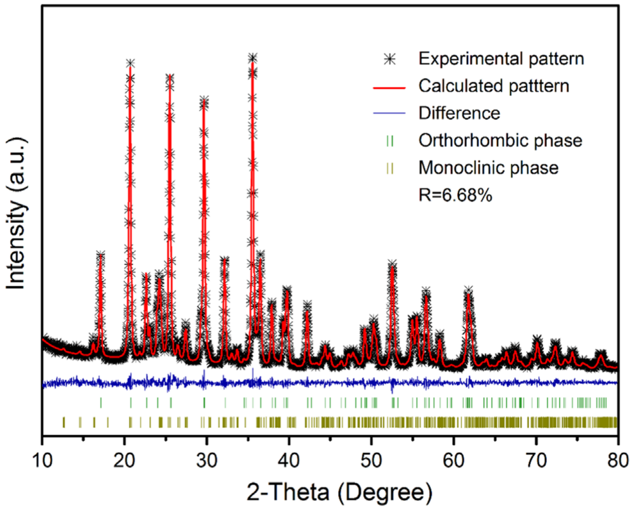

Figure 1 X-ray diffraction pattern with Rietveld refinement of 8$LiFePO_4\cdot Li_3V_2(PO_4)_3$/C. The crosses denote the observed data and the continuous red line covered above represents the fitted pattern. The difference pattern is also shown. The bottom vertical bars indicate the Bragg position of $LiFePO_4$ and $Li_3V_2(PO_4)_3$, respectively.

Results and discussion

Figure 1 shows the powder X-ray diffraction (XRD) pattern of the prepared 8$LiFePO_4\cdot Li_3V_2(PO_4)_3$/C composite. The Rietveld refinement method (Jade 9.0 software, MDI, USA) was used to refine the X-ray diffraction patterns to analyze the crystal structures and phases of the material. The atomic positions of $LiFePO_4$ and $Li_3V_2(PO_4)_3$ in 8$LiFePO_4\cdot Li_3V_2(PO_4)_3$/C composite are listed in Table S1. The composites were composed of orthorhombic $LiFePO_4$ (space group *Pnma*, 162064-ICSD) and monoclinic $Li_3V_2(PO_4)_3$ (space group *P2₁/n*, 98362-ICSD), with no evidence of undesired parasitic phases (such as Fe_2P or V_2O_3) nor crystalline carbon diffraction peak. Moreover, the sharp peaks in the patterns indicate that the composite material is well crystallized. Table 1 shows the refined cell parameters of the $LiFePO_4$ and $Li_3V_2(PO_4)_3$ in the prepared sample, which correspond well to the previously reports [7,15,41]. The observed and calculated patterns match well, and the reasonably small *R* factor (6.68%) suggests that the refinement results are convincible. The mass

Table 1 Refined unit cell lattice parameters of $LiFePO_4$ and $Li_3V_2(PO_4)_3$ in $8LiFePO_4 \cdot Li_3V_2(PO_4)_3/C$ and the standard data of $LiFePO_4$ (162064-ICSD) and $Li_3V_2(PO_4)_3$ (98362-ICSD).

Sample	Lattice parameters					Phase content (wt%)	R (%)
	a (nm)	b (nm)	c (nm)	β (°)	V (nm^3)		
LFP in 8LFP · LVP	1.03144	0.60021	0.46940	90.0000	0.2906	75.7	6.68
LFP	1.03182	0.60037	0.46937	90.0000	0.2908	–	–
LVP in 8LFP · LVP	0.85940	0.86027	1.20468	90.5359	0.8906	24.3	6.68
LVP	0.86056	0.85917	1.20380	90.6090	0.8899	–	–

content of $LiFePO_4$ and $Li_3V_2(PO_4)_3$ determined by multiphase refinement is 75.7±1.2 wt% and 24.3±1.2 wt%, respectively. The unit cell volume of $LiFePO_4$ in the $8LiFePO_4 \cdot Li_3V_2(PO_4)_3/C$ composite decreases obviously, compared with that of pure phase $LiFePO_4$, which may be attributed to the V doping into the $LiFePO_4$ host lattice because the ionic radius of V^{3+} (0.74 Å) is smaller than that of Fe^{2+} (0.78 Å). However, the cell volume of $Li_3V_2(PO_4)_3$ in the $8LiFePO_4 \cdot Li_3V_2(PO_4)_3/C$ composite increases compared with the pristine $Li_3V_2(PO_4)_3$, suggesting that Fe also entered into the $Li_3V_2(PO_4)_3$ host lattice. The above results indicate that most of the iron and vanadium in the raw materials tend to form the $LiFePO_4$ and $Li_3V_2(PO_4)_3$ phases, and a small amount of Fe and V as the dopants enter into the lattice of $Li_3V_2(PO_4)_3$ and $LiFePO_4$ (mutual doping), respectively. Furthermore, the calculated weight percent of $LiFePO_4$ and $Li_3V_2(PO_4)_3$ phases for the sample deviates a little from the theoretical value, which is attributed to the mutual doping between the two materials. In earlier literatures [13,21,42,43], the $LiFePO_4$ doping with V^{3+} as well as the $Li_3V_2(PO_4)_3$ doping with Fe^{2+} are beneficial to improve their electron conductivity and electrochemical performance. XRD patterns of the prepared pristine $LiFePO_4/C$ and $Li_3V_2(PO_4)_3/C$ samples are illustrated in Figure S1. All diffraction reflexes can be well indexed to orthorhombic $LiFePO_4$ (space group *Pnma*, in accordance with ICSD no. 162064) and monoclinic $Li_3V_2(PO_4)_3$ (space group $P2_1/n$, in accordance with ICSD no. 98362), respectively, and no evidence of secondary phases or crystalline carbon diffraction reflexes is present.

The morphological and microstructure features of the prepared materials were investigated by field emission scanning electron microscopy (FESEM) and transmission electron microscopy (TEM), as shown in Figure 2. The low-magnification FESEM image (Figure 2a) reveals the composite is composed of loose and interconnected nanoflakes. The nanoflake particles are homogenously dispersed, and the shape of the nanoflakes is quite uniform. Figure S2 shows the SEM images of pristine $LiFePO_4/C$ and $Li_3V_2(PO_4)_3/C$ prepared by the similar strategy. The $LiFePO_4$ is composed of irregular nanoparticles and $Li_3V_2(PO_4)_3$ is constructed by loosely interconnected nanoflakes, which are in good accordance with the previous reports [10,16]. The result indicates the existence of $Li_3V_2(PO_4)_3$ in the $8LiFePO_4 \cdot Li_3V_2(PO_4)_3/C$ composite is helpful to obtain uniform structures, although the addition amount of $Li_3V_2(PO_4)_3$ is only 1/9 in molar ratio. According to the elemental mapping result, the distribution of C, V, and Fe is very uniform within the aggregates, which suggest the high homogeneity of the composite (Figure S3). Figure 2b gives a much clear picture of the composite. The $8LiFePO_4 \cdot Li_3V_2(PO_4)_3/C$ nanoflakes are approximately 20-50 nm in thickness and have an in-plane extension of about 1-2 μm. The high magnification TEM image (Figure 2c) reveals that the single $8LiFePO_4 \cdot Li_3V_2(PO_4)_3/C$ nanoflake is composed of many infinitesimal interconnected nanoparticles with diameter of 30 – 100 nm and a multiplicity of mesoporous channels with a uniform pore size of 10-50 nm. Figure 2d shows the high angle annular dark field scanning transmission electron microscopy (HAADF-STEM) images of nanoflakes, which confirms homogeneous distribution of V and Fe in the prepared sample. The result indicates the high efficiency of making $LiFePO_4$ and $Li_3V_2(PO_4)_3$ composite, rather than a simple macroscopical mixing. Furthermore, the coated carbon distributes evenly on the particle surface (Figure S3). According to the C-S analysis, the mass content of carbon is about 4.86%. The HRTEM images of the prepared sample are provided as shown in Figure 2e and f. The carbon layer with a thickness of about 5 nm can also be observed (inset of Figure 2e). The Fourier transform (FFT) images of regions (inset of Figure 2f) show the diffraction spots of $LiFePO_4$, and $Li_3V_2(PO_4)_3$, respectively. By comparing interplanar distances measured from HRTEM with the theoretical value, the existence of $LiFePO_4$ and $Li_3V_2(PO_4)_3$ is confirmed, consistent with the results from XRD crystal analysis.

In this work, oleic acid acts as a surfactant that directs the growth orientation of $8LiFePO_4 \cdot Li_3V_2(PO_4)_3/C$ nanoflakes. Oleic acid ($CH_3(CH_2)_7CH{=}CH(CH_2)_7COOH$), a monounsaturated omega – 9 fatty acid found in various animal and vegetable sources, has been well known as a surfactant with carboxyl group, long alkyl chain and unsaturated bond. The carboxyl group in oleic acid could attach on the surface of nanoparticles. On the other hand, the presence of the long alkyl chain and unsaturated bond in oleic acid provides significant hydrophobicity to the nanoparticles and is beneficial for a good interfacial bonding between the nanoparticles and the matrix [35,36,44]. Such an oleic acid surfactant can extend its tail in molten paraffin media in a manner similar to self-assembly approach [44]. As a result, the nanoparticles modified by oleic acid can grow preferentially along specific directions to form the $8LiFePO_4 \cdot Li_3V_2(PO_4)_3/C$ nanoflakes. Moreover, the $8LiFePO_4 \cdot Li_3V_2(PO_4)_3$ composite is carbon coated due to the *in-situ* decomposition of oleic acid on the active material, which may beneficial for the electron transportation for lithium ion batteries [20,34].

The existence of carbon in the composite has been confirmed by Raman scattering spectrum result (Figure 3a). The two broad bands at 1330 cm^{-1} and 1610 cm^{-1} can be assigned to the D-band (disorder-induced phonon mode) and G-band

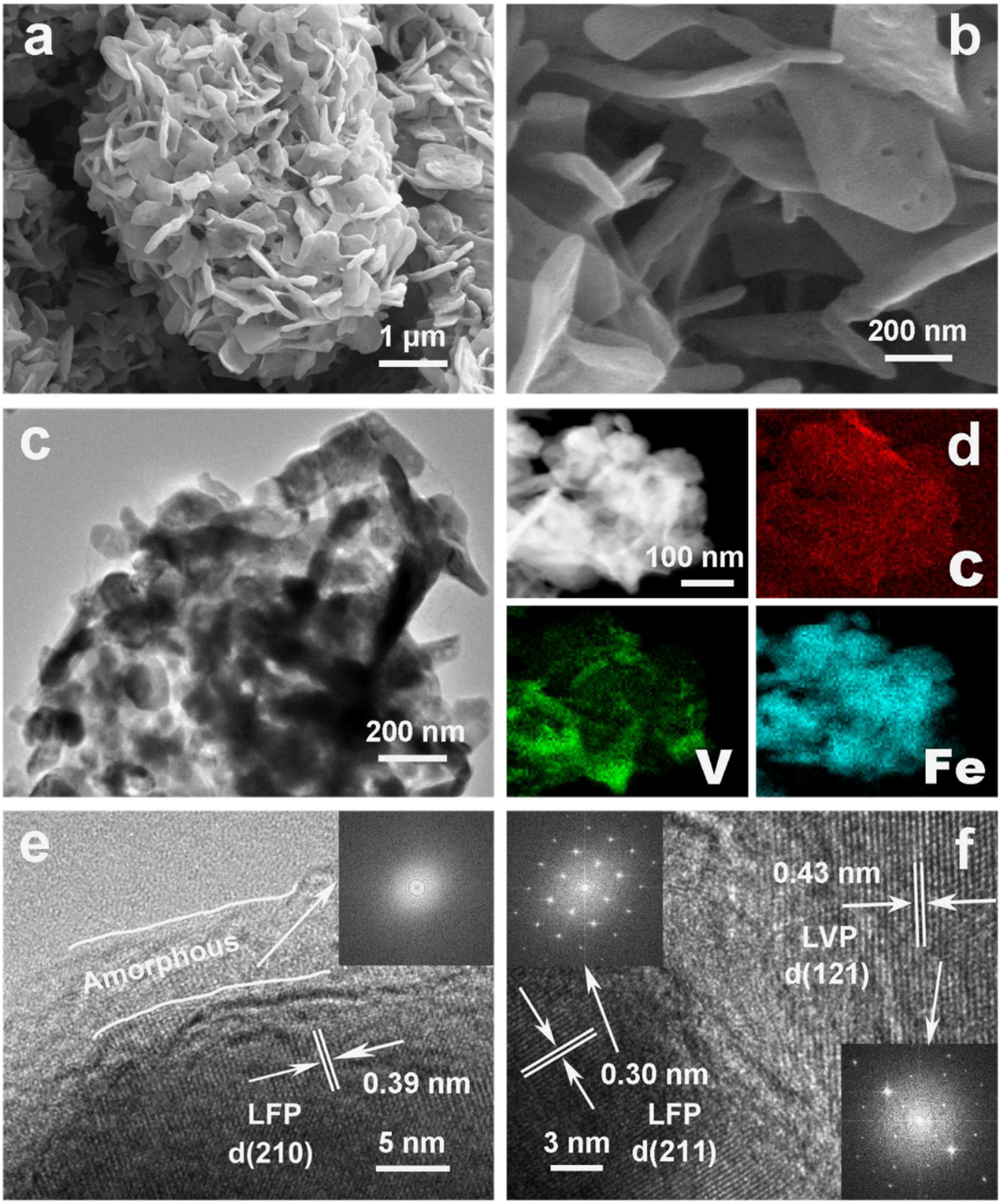

Figure 2 (a, b) FESEM images, (c) TEM image, (d) STEM-HAADF images, (e, f) HRTEM image of the as-synthesized $8LiFePO_4 \cdot Li_3V_2(PO_4)_3/C$ nanoflakes; inset of (e) is the Fourier transform (FFT) image of coated carbon layer, inset of (f) are the Fourier transform (FFT) images of the corresponding area.

(graphite band), respectively, indicating the existence of the carbon layer in the material and the partial graphitization of the deposited carbon [17,45]. The peak intensity ratio between the D- and G-bands (ID/IG) generally provides a useful index about the degree of crystallinity of various carbon materials. In general, the high ordering degree of the carbon materials have high ID/IG values [46]. The intensity ratio of ID/IG in the as-synthesized $8LiFePO_4 \cdot Li_3V_2(PO_4)_3/C$ nanoflakes is around 0.97, indicating a relatively high degree of graphitization, which will be beneficial for achieving better electronic conductivity for the composite material [47-49].

The nitrogen adsorption-desorption analysis was carried out to investigate the porosity of the $8LiFePO_4 \cdot Li_3V_2(PO_4)_3/C$ nanoflakes and the results are shown in Figure 3b. The isotherm can be described as type II with a H3 hysteresis loop, which indicates the slit-shaped pores in the composite. According to the Brunauer-Emmett-Teller (BET) method, the surface area of the $8LiFePO_4 \cdot Li_3V_2(PO_4)_3/C$

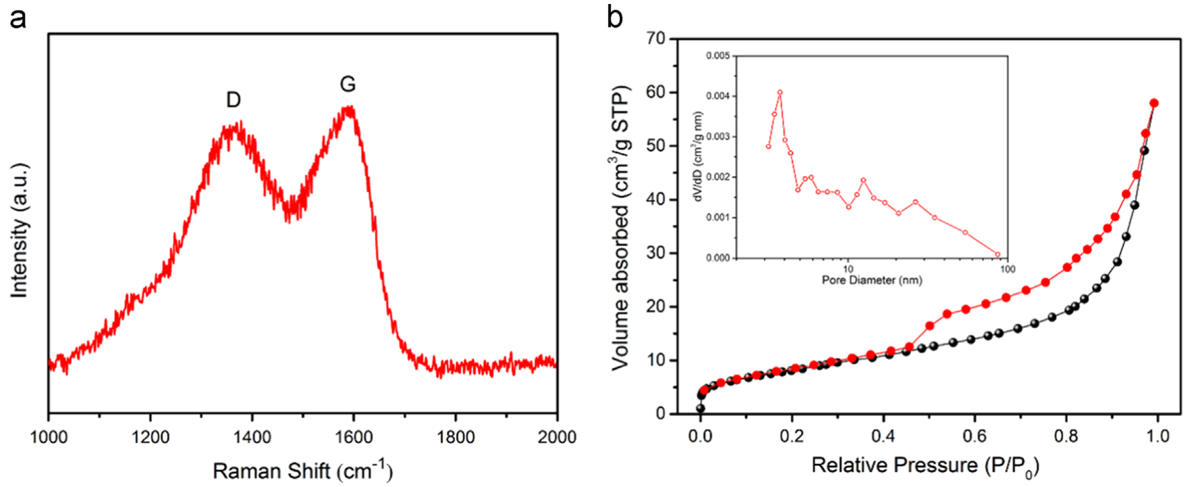

Figure 3 (a) Raman scattering spectrum of the $8LiFePO_4 \cdot Li_3V_2(PO_4)_3/C$ nanoflakes. (b) Nitrogen adsorption-desorption isotherm and the corresponding pore-size-distribution (inset) of the $8LiFePO_4 \cdot Li_3V_2(PO_4)_3/C$ nanoflakes.

nanoflakes is about 30.21 $m^2\,g^{-1}$. The Barret-Joyner-Halenda (BJH) pore-size-distribution curve (inset of Figure 3b) indicates that the pore sizes in $8LiFePO_4 \cdot Li_3V_2(PO_4)_3/C$ mainly range from 3 to 30 nm, and pore volume of 0.11 $cm^3\,g^{-1}$. The relative high surface area and porous structures are believed to be of advantages of providing more active sites for lithium intercalation/deintercalation and easy path way for electrolyte penetration [50,51].

The as-prepared $8LiFePO_4 \cdot Li_3V_2(PO_4)_3/C$ composite nanoflakes, pristine $LiFePO_4/C$ and $Li_3V_2(PO_4)_3/C$ were assembled into coin cells to evaluate their electrochemical performance. Figure 4a shows the first three successive CV curves of the composite electrodes the voltage range of 2.5−4.3V (vs. Li/Li^+) at a scan rate of 0.1 mV s^{-1}. Four couples of redox peaks are observed on the CV curves. The pair peaks at 3.54 V/3.33 V are ascribed to the oxidation and reduction of Fe^{2+}/Fe^{3+} from $LiFePO_4$ [6, 7], whereas the other three redox couple peaks at 3.60 V/3.57 V, 3.69 V/3.65 V, and 4.10 V/4.04 V are associated with the V^{3+}/V^{4+} redox reaction for $Li_3V_2(PO_4)_3$ [10]. The redox peaks for the composite electrode are in good accordance with those for pristine $LiFePO_4$ and $Li_3V_2(PO_4)_3$ (Figure S4a and S5a). The oxidation peak of $Li_3V_2(PO_4)_3$ around 3.6 V is annexed by the oxidation peak of $LiFePO_4$ at 3.54 V. This phenomenon is also reported in other $LiFePO_4/Li_3V_2(PO_4)_3$ composite electrode materials [21,23]. Moreover, the first three successive CV curves are almost identical, demonstrating the good stability of the electrode material. And the little potential difference between the anodic and cathodic peaks for $LiFePO_4$ indicates the low polarization of the $LiFePO_4/Li_3V_2(PO_4)_3$ composite [22,26].

Figure 4b shows the charge-discharge profiles of the initial cycles for the composite electrode, which exhibit four charge/discharge plateaus. The multiple plateaus indicate the multiple steps of lithium ions intercalation/de-intercalation process. The charge plateaus located around 3.60 V, 3.69 V and 4.10 V can be identified as the extraction of lithium ions from $Li_3V_2(PO_4)_3$ (Figure S4b), and the plateau at 3.54 V is attributed to the lithium extraction from $LiFePO_4$ (Figure S5b). Meanwhile, the three discharge plateaus located around 4.04 V, 3.65 V, and 3.57 V are attributed to the insertion of Li^+ ions, accompanied by the phase transition from $LiV_2(PO_4)_3$ to $Li_3V_2(PO_4)_3$. And the plateaus at 3.33 V is attributed to the lithium insertion into $FePO_4$ to produce $LiFePO_4$ [13,15,52]. The potentials of the charge/discharge plateaus are in good agreement with the CV results (Figure 4a). In addition, the initial coulombic efficiency of the as-prepared composite cathode material is 97%, and a high initial discharge capacity of 161.5 mAh g^{-1} can be delivered within the voltage range of 2.5−4.3 V at a current density of 0.1 C, which is very close to the theoretical capacity for the composite.

Figure 4c shows the cycling behavior of the $8LiFePO_4 \cdot Li_3V_2(PO_4)_3/C$ electrode at the current density of 170 mA g^{-1} in the voltage range of 2.5−4.3 V (vs. Li/Li $^+$). The composite electrodes deliver a maximum specific discharge capacity of 153.1 mAh g^{-1} and can retain of 93.86% of its capacity after 500 cycles. The average capacity fading rate is 0.1% per cycle. The coulombic efficiency is above 98% during the whole cycling process, confirming the good reversibility of the electrode materials [33, 52].

Electrochemical impedance spectroscopy (EIS) measurements of $8LiFePO_4 \cdot Li_3V_2(PO_4)_3/C$ composite electrode after different cycles at 1 C rate were carried out in the frequency ranging from 100 kHz to 0.01 Hz (Figure 4d). All the Nyquist plots are composed of a small intercept in the highest frequency range, a depressed semicircle in the high-middle frequency region, and a slanted line in the low-frequency region. The high frequency intercept at the Z_{real} axis corresponds to the Ohmic resistance of the cell, including the resistance of electrolyte, separator, current collector and so on [53]. The semicircle is mainly ascribed to the charge transfer reaction at the electrode/electrolyte interface, and the slanted line is ascribed to the slow diffusion process of lithium ions in the bulk of the electrode material [54,55]. Inset in Figure 4d shows the equivalent circuit model proposed for the interpretation of the impedance spectra. R_s is the combination of electrolyte resistance and Ohmic resistances of cell components. R_{ct} and CPE represent the charge transfer resistance and double-layer capacitance, respectively. Z_w represents the diffusion-

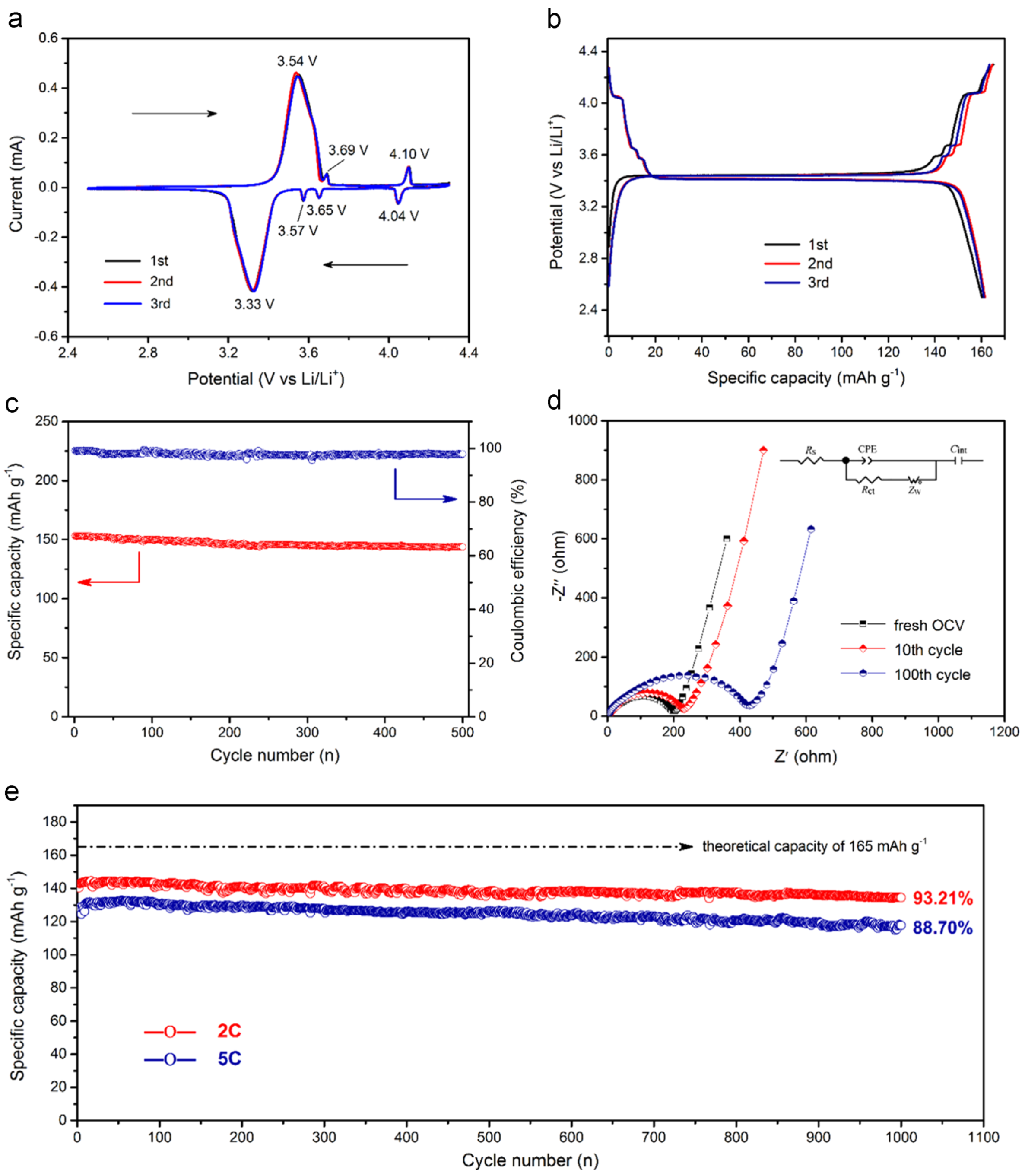

Figure 4 Electrochemical characterizations of the $8LiFePO_4 \cdot Li_3V_2(PO_4)_3/C$ nanoflakes: (a) the first three successive cyclic voltammograms curves at a scan rate of 0.1 mV s^{-1} in a voltage range of 2.5-4.3 V; (b) the first three charge-discharge profiles at a current density of 0.1 C (1 C=170 mA g^{-1}); (c) cycling performance at the current density of 1 C between the voltage range of 2.5-4.3 V; (d) Nyquist plots of the sample after different cycles; (e) long-term cycling performance of the samples at 2 C and 5 C.

controlled Warburg impedance and C_{int} indicates the capacitance caused by the accumulation or loss of Li^+ in the crystal of electrode material. The simulated charge transfer resistances (R_{ct}) of the $8LiFePO_4 \cdot Li_3V_2(PO_4)_3/C$ samples are 158.2 Ω for the fresh electrode. After 10 and 100 cycles, their corresponding charge transfer resistances are 175.4 Ω, and 327.1 Ω, respectively (Table S2). The charge transfer resistance in the 10th and 100th cycle increase slightly. The charge transfer resistance increase is also reported in other composite electrode materials [47,48,56]. However, the little charge transfer resistance increase can be attributed to the carbon coated $8LiFePO_4 \cdot Li_3V_2(PO_4)_3$ nanoflake structures, which can facilitate the generated electron transportation. Besides, the Nyquist plots (Figure S4d and S5d) show that the charge transfer resistance (R_{ct}) of both pristine $LiFePO_4/C$ and $Li_3V_2(PO_4)_3/C$ electrodes are much bigger than the $8LiFePO_4 \cdot Li_3V_2(PO_4)_3/C$ composite electrode (Table S2 and S3). This indicates that making the composites with novel nanostructures indeed improves the charge transfer kinetics.

The long-term cycling performance at high rate is a critical requirement for high-power LIB applications such as plug-in hybrid electric vehicles (PHEV) and plug-in electric vehicle (PEV). Figure 4e shows the cycling performance of $8LiFePO_4 \cdot Li_3V_2(PO_4)_3/C$ nanoflakes electrode for 1000 cycles. The capacity increase in the initial cycles can be attributed to the activation process due to the gradual wetting of the electrode materials by electrolyte, which is commonly observed in various nanocomposite electrodes [48,54,57]. The composite electrodes can deliver the maximum specific discharge capacities of 144.3 and 132.8 mAh g^{-1} at 2 C and 5 C, respectively. After 1000 cycles, it still can retain 134.5 mA h g^{-1} at 2 C, 94% of its original capacity. And the composite electrode delivers 117.8 mA h g^{-1} after 1000 cycles at 5 C, with an average capacity fading rate of 0.0113% per cycle. The results demonstrate the excellent long-term cyclic stability of the $8LiFePO_4 \cdot Li_3V_2(PO_4)_3/C$ nanoflakes compared with the pristine $LiFePO_4/C$ (Figure S4e) and $Li_3V_2(PO_4)_3/C$ (Figure S5e). The superior cycling performance can be attributed to the carbon coated $8LiFePO_4 \cdot Li_3V_2(PO_4)_3/C$ porous composite, in which the carbon can improve the conductivity of the electron and improve the stability of the electrode materials. Moreover, the porous structures can provide buffer space for the volume changes, keeping the structural integrity.

Figure 5 shows the rate capability of $8LiFePO_4 \cdot Li_3V_2(PO_4)_3/C$ nanoflake composite and their corresponding discharge/charge curves in the potential range of 2.5–4.3 V. As shown in Figure 5a, the $8LiFePO_4 \cdot Li_3V_2(PO_4)_3/C$ nanoflakes electrode exhibit superior rate capability. It can release the discharge capacities of 161.5, 157.3, 152.9, 145.9, and 132.8 mAh g^{-1} at 0.1 C, 0.5 C, 1 C, 2 C, and 5 C, respectively. Even at 10 C, it still delivers a capacity of 118.6 mAh g^{-1}. When the current was reset to 1 C, a specific capacity of 151.1 mAh g^{-1} could be restored. It is worth noting that the composite electrode exhibits good cyclic stability at all the rates. Figure 5b shows the corresponding charge-discharge curves at various rates. Even at 10 C, the discharge/charge plateaus can be clearly detected. The rate performance of the $8LiFePO_4 \cdot Li_3V_2(PO_4)_3/C$ nanoflakes electrode is much better than the pristine $LiFePO_4/C$ and $Li_3V_2(PO_4)_3/C$ electrodes (Figure S4d and S5d). The nanoscaled thickness of the nanoflakes can greatly reduced the lithium ion diffusion distance, and the porous structures can provide the reaction sites and easy electrolyte penetration path ways. Furthermore, the carbon coating can improve the electron conductivity of the electrode materials.

In order to evaluate the structural stability of the $8LiFePO_4 \cdot Li_3V_2(PO_4)_3/C$ composite nanoflakes, the electrode materials after 1000 cycles were collected and studied by XRD and SEM techiniques. As can be seen in Figure S6, the XRD pattern of the electrode materials after 1000 cycles has no significant difference and both exhibit the main characteristic peaks of original $8LiFePO_4 \cdot Li_3V_2(PO_4)_3$. Moreover, the nanoflakes can be well retained after 1000 cycles at 5 C (Figure S7), which demonstrate their good structural stability upon cycling.

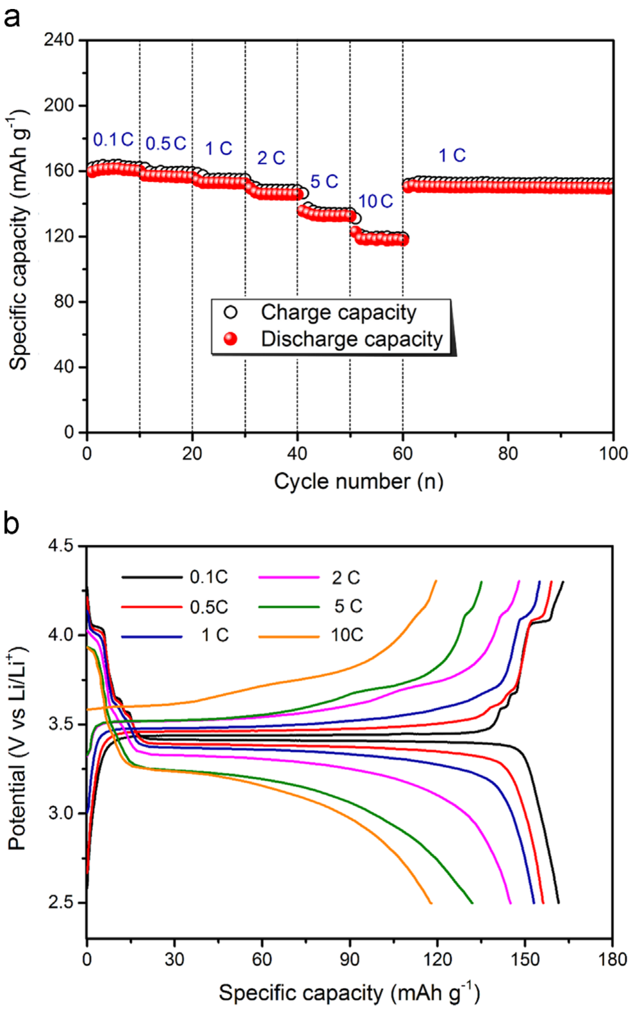

Figure 5 (a) Rate performance of the $8LiFePO_4 \cdot Li_3V_2(PO_4)_3/C$ electrode at various rates, and (b) their corresponding charge-discharge profiles.

In order to further investigate the effect of fast ionic conducting $Li_3V_2(PO_4)_3$ additive on the electrochemical properties of $LiFePO_4$, the apparent diffusion coefficient of lithium ions is determined by cyclic voltammetry technique. Figure 6a shows the CV curves of the prepared sample at scan rates of 0.05, 0.1, 0.25, 0.5, 0.75, 1.0 mV s^{-1} in the voltage range of 3.0–4.3 V. As shown in Figure 6a, with the increase of the scan rates, the anodic peaks shift right and the corresponding cathodic peaks move left, which indicates larger polarization at high scan rates. And the intensities of redox peaks increase with increasing scan rate. From Figure 6b, the peak current (I_p) has a linear relationship with the square root of scan rate ($v^{1/2}$), indicating diffusion-controlled process [53,58]. For the semi-infinite and finite diffusion, the peak current is proportional to the square root of the scan rate and can be expressed by the classical Randles Sevchik method (Eq. (2)) [58].

$$I_p = 2.69 \times 10^5 n^{3/2} A D^{1/2} v^{1/2} C_0^* \tag{2}$$

Where I_p is the peak current (A), n is the number of electrons per species reaction (for Li^+, $n=1$), A is the active surface area of the electrode (here 1.131 cm^2 is used for simplicity), D is the diffusion coefficient of lithium ion (cm^2 s^{-1}), v is the scan rate (V s^{-1}), and C_0^* is the is the concentration of lithium ions corresponding to the different specific electrochemical reaction steps (mol cm^{-3}). Because the situation in this study is complex as the diffusion might be affected by the tortuous pass in the composite electrodes. We recommend the effective diffusion coefficients (D_{se}) herein just for the solid-state cathode electrode, and we used n_e and C_{0e}^* as effective one respectively, and the values are listed (Table S4). Based on Eq. (2) and the slope of I_p versus $v^{1/2}$ plots in Figure 6b, the diffusion coefficients of lithium ion in solid state composite are calculated and listed in Table 2. It can be seen that the values of D_{se} for the solid state composite are in the magnitude of 10^{-9} to 10^{-10} cm^2 s^{-1} and close to each other. The Li-ion diffusion coefficients of $8LiFePO_4 \cdot Li_3V_2(PO_4)_3/C$ composite electrode after different cycles, listed in Table S5, are also calculated based on the Equation S1 and linear relationship between Z' vs. $\omega^{-1/2}$ at low-frequency region (Figure S8). The values are at least 3 orders of magnitude larger than that of $LiFePO_4$ (10^{-13} to 10^{-15} cm^2 s^{-1}) [6], $LiMnPO_4$ (1.5×10^{-13} cm^2 s^{-1}) [24], and $LiFe_xMn_{1-x}PO_4$ (10^{-15} to 10^{-17} cm^2 s^{-1}) [14], and are comparable with that of $Li_3V_2(PO_4)_3$ [33,53], $xLiFePO_4 \cdot LiVPO_4F$ composite [59], and $xLi_3V_2(PO_4)_3 \cdot LiVPO_4F$ composite [58]. The result demonstrate that the lithium ion diffusion coefficient has been greatly improved by making $Li_3V_2(PO_4)_3/LiFePO_4$ composite, although the amount of $Li_3V_2(PO_4)_3$ is quite small.

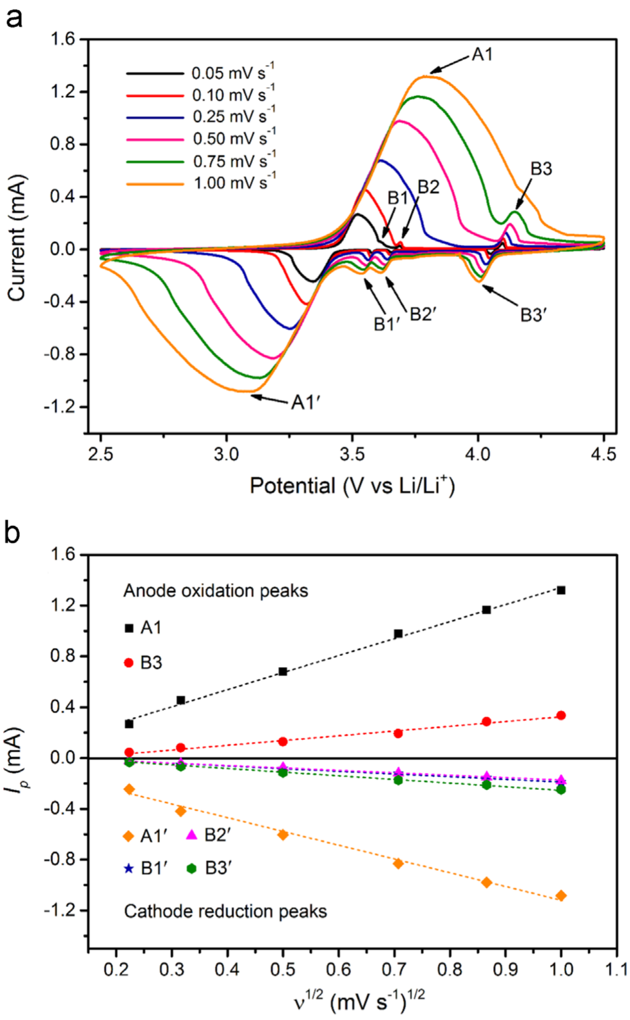

Figure 6 (a) The CV curves of the $8LiFePO_4 \cdot Li_3V_2(PO_4)_3/C$ composite nanoflakes at various scan rates; (b) The line relationship of the peak current (I_p) versus square root of scan rate ($\nu^{1/2}$).

According to the above results, the excellent electrochemical performance of $8LiFePO_4 \cdot Li_3V_2(PO_4)_3/C$ nanoflakes, including high capacity, good cyclic stability and rate capability can be ascribed to the novel carbon coated $8LiFePO_4 \cdot Li_3V_2(PO_4)_3/C$ nanoflake composite: (1) the nanoscaled thickness of the nanoflakes reduce the lithium-ion diffusion distance and the porous structure further enlarges the contact area between electrode and electrolyte; (2) the ample space between nanoflakes provides the easy path for electrolyte penetration and better accommodates the volume change during charge/discharge process; (3) The mutual cross-doping between $LiFePO_4$ and $Li_3V_2(PO_4)_3$ is beneficial to improve their conductivity and lithium ion diffusion coefficient; (4) the carbon coating on the composite nanoflakes would improve the electron transportation and better keep the structural integrity.

Conclusions

Uniform $8LiFePO_4 \cdot Li_3V_2(PO_4)_3/C$ nanoflake composite has been synthesized by a one-pot, solid-state method in a molten hydrocarbon, which is cost-effective, and environmental benign for large scale production. The $LiFePO_4$ and $Li_3V_2(PO_4)_3$ are homogenously distributed within the

Table 2 The diffusion coefficients of lithium-ion in composite electrode calculated from CV based on the classical Randles Sevchik equation.

State	Anodic oxidation process		Cathodic reduction process	
	Peak	D_{se} (cm^2 s^{-1})	Peak	D_{se} (cm^2 s^{-1})
$8FePO_4 \cdot Li_3V_2(PO_4)_3$	*A1*	4.6×10^{-10}	*A1′*	2.9×10^{-10}
$8FePO_4 \cdot Li_{2.5}V_2(PO_4)_3$	*B1*	—	*B1′*	6.4×10^{-9}
$8FePO_4 \cdot Li_2V_2(PO_4)_3$	*B2*	—	*B2′*	9.4×10^{-9}
$8FePO_4 \cdot LiV_2(PO_4)_3$	*B3*	1.6×10^{-9}	*B3′*	8.7×10^{-9}

nanoflakes and are carbon coated. Moreover, the lithium ion diffusion coefficient is greatly improved in the composite as compared to $LiFePO_4$ due to the mutual doping effect. As cathode materials for lithium ion batteries, the resulting $8LiFePO_4 \cdot Li_3V_2(PO_4)_3$/C nanoflakes exhibit excellent electrochemical performances, including high reversible capacity, excellent cyclic stability and good rate capability. The synthesis strategy may also be used to explore other nanocomposites, especially for high temperature synthesis.

Acknowledgments

This work was supported by the National High Technology Research and Development Program of China (863 Program) (No. 2013AA110106), the National Natural Science Foundation of China (Nos. 51374255, 51302323), Supported by Program for New Century Excellent Talents in University (NCET−13−0594), Supported by Research Fund for the Doctoral Program of Higher Education of China (No. 201301621200), Supported by Natural Science Foundation of Hunan Province, China (14JJ3018), Supported by the Fundamental Research Funds for the Central Universities of Central South University(No. 2015zzts179).

Appendix A. Supplementary material

Supplementary data associated with this article can be found in the online version at http://dx.doi.org/10.1016/j.nanoen.2016.02.002.

References

[1] N. Kamaya, K. Homma, Y. Yamakawa, M. Hirayama, R. Kanno, M. Yonemura, T. Kamiyama, Y. Kato, S. Hama, K. Kawamoto, A. Mitsui, Nature Mater. 10 (2011) 682-686.

[2] M.S. Whittingham, Chem. Rev. 114 (2014) 11414-11443.

[3] E. Uchaker, G. Cao, Nano Today 9 (2014) 499-524.

[4] H. Li, Z. Wang, L. Chen, X. Huang, Adv. Mater. 21 (2009) 4593-4607.

[5] C. Masquelier, L. Croguennec, Chem. Rev. 113 (2013) 6552-6591.

[6] Y. Zhao, L. Peng, B. Liu, G. Yu, Nano Lett. 14 (2014) 2849-2853.

[7] L. Wang, X. He, W. Sun, J. Wang, Y. Li, S. Fan, Nano Lett. 12 (2012) 5632-5636.

[8] D. Choi, D. Wang, I.T. Bae, J. Xiao, Z. Nie, W. Wang, V. V. Viswanathan, Y.J. Lee, J.G. Zhang, G.L. Graff, Z. Yang, J. Liu, Nano Lett. 10 (2010) 2799-2805.

[9] L. Shen, H. Li, E. Uchaker, X. Zhang, G. Cao, Nano Lett. 12 (2012) 5673-5678.

[10] A.Q. Pan, D.W. Choi, J.G. Zhang, S.Q. Liang, G.Z. Cao, Z. M. Nie, B.W. Arey, J. Liu, J. Power Sources 196 (2011) 3646-3649.

[11] Y. Zhou, X. Rui, W. Sun, Z. Xu, Y. Zhou, W.J. Ng, Q. Yan, E. Fong, ACS Nano 9 (2015) 4628-4635.

[12] A.K. Padhi, K.S. Nanjundaswamy, J.B. Goodenough, J. Electrochem. Soc. 144 (1997) 1188.

[13] L.L. Zhang, G. Liang, A. Ignatov, M.C. Croft, X.Q. Xiong, I. M. Hung, Y.H. Huang, X.L. Hu, W.X. Zhang, Y.L. Peng, J. Phys. Chem. C 115 (2011) 13520-13527.

[14] B. Ding, P. Xiao, G. Ji, Y. Ma, L. Lu, J.Y. Lee, ACS Appl. Mater. Interfaces 5 (2013) 12120-12126.

[15] A. Vu, A. Stein, Chem. Mater. 23 (2011) 3237-3245.

[16] D.W. Choi, D.H. Wang, V.V. Viswanathan, I.T. Bae, W. Wang, Z. M. Nie, J.G. Zhang, G.L. Graff, J. Liu, Z.G. Yang, T. Duong, Electrochem. Commun. 12 (2010) 378-381.

[17] X.L. Wu, L.Y. Jiang, F.F. Cao, Y.G. Guo, L.J. Wan, Adv. Mater. 21 (2009) 2710-2714.

[18] C. Ban, W.J. Yin, H. Tang, S.H. Wei, Y. Yan, A.C. Dillon, Adv. Energy Mater. 2 (2012) 1028-1032.

[19] J. Wang, X. Sun, Energy Environ. Sci. 8 (2015) 1110-1138.

[20] J. Wang, X. Sun, Energy Environ. Sci. 5 (2012) 5163-5185.

[21] Y. Guo, Y.D. Huang, D.Z. Jia, X.C. Wang, N. Sharma, Z.P. Guo, X.C. Tang, J. Power Sources 246 (2014) 912-917.

[22] L. Wang, Z. Li, H. Xu, K. Zhang, J. Phys. Chem. C 112 (2008) 308-312.

[23] F. Wang, J. Yang, Y.N. NuLi, J.L. Wang, Electrochim. Acta 103 (2013) 96-102.

[24] L. Zhang, Q. Qu, L. Zhang, J. Li, H. Zheng, J. Mater. Chem. A 2 (2014) 711-719.

[25] X. Zhang, R.S. Kühnel, H. Hu, D. Eder, A. Balducci, Nano Energy 12 (2015) 207-214.

[26] M.R. Yang, W.H. Ke, S.H. Wu, J. Power Sources 165 (2007) 646-650.

[27] J.F. Zhang, C. Shen, B. Zhang, J.C. Zheng, C.L. Peng, X. W. Wang, X.B. Yuan, H. Li, G.M. Chen, J. Power Sources 267 (2014) 227-234.

[28] J.C. Zheng, X.H. Li, Z.X. Wang, S.S. Niu, D.R. Liu, L. Wu, L. J. Li, J.H. Li, H.J. Guo, J. Power Sources 195 (2010) 2935-2938.

[29] S. Zhong, L. Wu, J. Liu, Electrochim. Acta 74 (2012) 8-15.

[30] Q.Y. An, F.Y. Xiong, Q.L. Wei, J.Z. Sheng, L. He, D.L. Ma, Y. Yao, L.Q. Mai, Adv. Energy Mater. 5 (2015) 1401963.

[31] C. Niu, J. Meng, X. Wang, C. Han, M. Yan, K. Zhao, X. Xu, W. Ren, Y. Zhao, L. Xu, Q. Zhang, D. Zhao, L. Mai, Nat. Commun. 6 (2015) 7402.

[32] Q. Zhang, E. Uchaker, S.L. Candelaria, G. Cao, Chem. Soc. Rev. 42 (2013) 3127-3171.

[33] Q. Wei, Q. An, D. Chen, L. Mai, S. Chen, Y. Zhao, K.M. Hercule, L. Xu, A. Minhas-Khan, Q. Zhang, Nano Lett. 14 (2014) 1042-1048.

[34] L.F. Shen, B. Ding, P. Nie, G.Z. Cao, X.G. Zhang, Adv. Energy Mater. 3 (2013) 1484-1489.

[35] M. Chen, W. Ding, Y. Kong, G. Diao, Langmuir 24 (2008) 3471-3478.

[36] Z. Deng, L. Cao, F. Tang, B. Zou, J. Phys. Chem. B 109 (2005) 16671-16675.

[37] J.Y. Chen, S. Simizu, S.A. Friedberg, J. Appl. Phys. 57 (1985) 3338-3340.

[38] A.Q. Pan, J.G. Zhang, Z.M. Nie, G.Z. Cao, B.W. Arey, G.S. Li, S.Q. Liang, J. Liu, J. Mater. Chem. 20 (2010) 9193-9199.

[39] A.Q. Pan, T. Zhu, H.B. Wu, X.W. Lou, , Chem. Eur. J. 19 (2013) 494-500.

[40] A.Q. Pan, H.B. Wu, L. Yu, X.W. Lou, Angew. Chem. 125 (2013) 2282-2286.

[41] C. Sun, S. Rajasekhara, Y. Dong, J.B. Goodenough, ACS Appl. Mater. Interfaces 3 (2011) 3772-3776.

[42] L. Wu, J. Lu, G. Wei, P. Wang, H. Ding, J. Zheng, X. Li, S. Zhong, Electrochim. Acta 146 (2014) 288-294.

[43] F. Omenya, N.A. Chernova, S. Upreti, P.Y. Zavalij, K.W. Nam, X.Q. Yang, M.S. Whittingham, Chem. Mater. 23 (2011) 4733-4740.

[44] P.K. Khanna, T.S. Kale, M. Shaikh, N.K. Rao, C.V. V. Satyanarayana, Mater. Chem. Phys. 110 (2008) 21-25.

[45] Z. Jian, W. Han, X. Lu, H. Yang, Y.S. Hu, J. Zhou, Z. Zhou, J. Li, W. Chen, D. Chen, L. Chen, Adv. Energy Mater. 3 (2013) 156-160.

[46] Y. Shi, J.Z. Wang, S.L. Chou, D. Wexler, H.J. Li, K. Ozawa, H. K. Liu, Y.P. Wu, Nano Lett. 13 (2013) 4715-4720.

[47] Y.S. Chen, D. Zhang, X.F. Bian, X.F. Bie, C.Z. Wang, F. Du, M. Jang, G. Chen, Y.J. Wei, Electrochim. Acta 79 (2012) 95–101.

[48] J. Liu, P.J. Lu, S. Liang, J. Liu, W. Wang, M. Lei, S. Tang, Q. Yang, Nano Energy 12 (2015) 709–724.

[49] L.F. Shen, X.G. Zhang, E. Uchaker, C.Z. Yuan, G.Z. Cao, Adv. Energy Mater. 2 (2012) 691–698.

[50] Q.B. Zhang, J.X. Wang, J.C. Dong, F. Ding, X.H. Li, B. Zhang, S. H. Yang, K.L. Zhang, Nano Energy 13 (2015) 77–91.

[51] L. Chai, J. Wang, H. Wang, L. Zhang, W. Yu, L. Mai, Nano Energy 17 (2015) 224–232.

[52] Y. Luo, X. Xu, Y. Zhang, Y. Pi, Y. Zhao, X. Tian, Q. An, Q. Wei, L. Mai, Adv. Energy Mater. 4 (2014) 1400107.

[53] R. Zhang, Y. Zhang, K. Zhu, F. Du, Q. Fu, X. Yang, Y. Wang, X. Bie, G. Chen, Y. Wei, ACS Appl. Mater. Interfaces 6 (2014) 12523–12530.

[54] G. Fang, J. Zhou, Y. Hu, X. Cao, Y. Tang, S. Liang, J. Power Sources 275 (2015) 694–701.

[55] S. Yoon, C. Jo, S.Y. Noh, C.W. Lee, J.H. Song, J. Lee, Phys. Chem. Chem. Phys. 13 (2011) 11060–11066.

[56] P.J. Lu, M. Lei, J. Liu, CrystEngComm 16 (2014) 6745–6755.

[57] J.X. Wang, Q.B. Zhang, X.H. Li, B. Zhang, L.Q. Mai, K.L. Zhang, Nano Energy 12 (2015) 437–446.

[58] J. Wang, Z. Wang, X. Li, H. Guo, X. Wu, X. Zhang, W. Xiao, Electrochim. Acta 87 (2013) 224–229.

[59] Y.C. Lin, G.T.K. Fey, P.J. Wu, J.K. Chang, H.M. Kao, J. Power Sources 244 (2013) 63–71.

Prof Shuquan Liang received his Ph.D. degree from Central South University (P.R. China) in 2000. He has been the Dean of School of Materials Science and Engineering in Central South University (CSU) since 2010. He is the winner of Monash University Engineering Sir John Medal. He hosted 5 state research projects including national 973 sub-project and national 863 project. He has published more than 60 papers in frontier journals. Currently, his main research interests include micro/nanostructured functional materials, nanocomposites and their energy storage and conversion devices.

Xinxin Cao received his Bachelor's degree in Materials science and Engineering from Central South University (CSU) in 2014. He is now a Ph.D. candidate in School of Materials science and Engineering, Central South University supervised by Prof. Shuquan Liang. His research focuses on the synthesis and application of nanomaterials and composites for clean energy storage, such as high-power/high-energy lithium ion batteries, and sodium ion batteries.

Yaping Wang received her B.E. degree in Mineral Process Engineering from Central South University in 2013 and she is currently a postgraduate student at the School of Materials Science and Engineering, Central South University (PR China). Her current research focuses on hollow-structured materials for electrochemical energy storage applications.

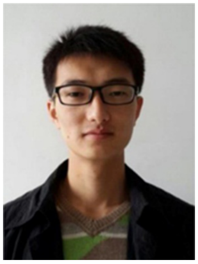

Yang Hu received his B.E. in Materials Science and Engineering from Central south university (PR China) in 2013. Currently, under the guidance of Prof. Liang, he is studying for his Ph.D. Degree in Materials Physics and Chemistry in Central South University. His current research interest is nanostructured cathode materials for lithium ion batteries.

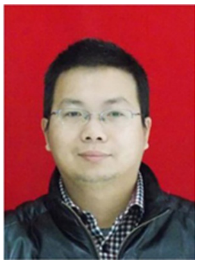

Anqiang Pan received his B. E. (2005) and D. Phil. (2011) degrees in Materials Physics and Chemistry from Central South University. He worked in Prof. Guozhong Cao's group at University of Washington as an exchange student (2008–2009). Then, he worked in PNNL as a visiting scholar in Dr. Ji-Guang Zhang and Dr. Jun Liu's group (2009–2011). He joined Prof. Xiongwen (David) Lou's group at Nanyang Technological University as a research fellow (2011-2012). He joined Central South University as a Sheng-Hua Professor in 2013. His current interests are on lithium ion batteries, and supercapacitors.

Guozhong Cao is Boeing-Steiner Professor of Materials Science and Engineering, Professor of Chemical Engineering, and Adjunct Professor of Mechanical Engineering at University of Washington, and also a Professor at Beijing Institute of Nanoenergy and Nanosystems, Chinese Academy of Sciences and Dalian University of Technology. His current research is focused on chemical processing of nanomaterials for energy related applications including solar cells, rechargeable batteries, supercapacitors, and hydrogen storage.